



# Extending the energy-power balance of Li-ion batteries using graded electrodes with precise spatial control of local composition

Chuan Cheng<sup>a,b,\*</sup>, Ross Drummond<sup>c,d</sup>, Stephen R. Duncan<sup>c,d</sup>, Patrick S. Grant<sup>a,d</sup>

<sup>a</sup> Department of Materials, University of Oxford, Oxford, OX1 3PH, UK

<sup>b</sup> Warwick Manufacturing Group, University of Warwick, Coventry, CV4 7AL, UK

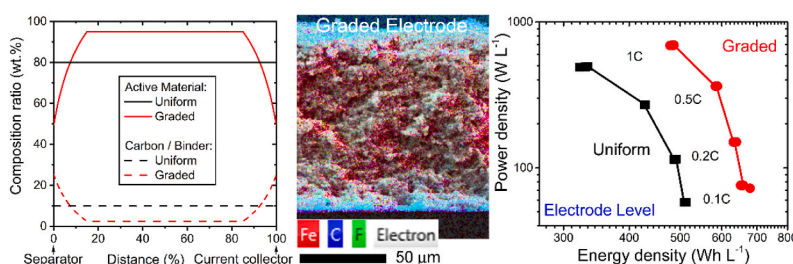
<sup>c</sup> Department of Engineering Science, University of Oxford, Oxford, OX1 3PJ, UK

<sup>d</sup> The Faraday Institution, Quad One, Harwell Campus, OX11 0RA, UK

## HIGHLIGHTS

- Energy-power trade-off in Li-ion cells is mitigated by composition graded electrodes.
- A composition gradient across an electrode thickness is realized by spray deposition.
- A heterogeneous electrode structure increases active materials utilization.
- A trapezoidal graded distribution increases the power performance of electrodes.
- C-rate response and cycling behaviour are enhanced by composition graded electrodes.

## GRAPHICAL ABSTRACT



## ARTICLE INFO

### Keywords:

Lithium-ion batteries  
Energy-power trade-off  
Electrode engineering  
Composition graded electrodes  
Additive manufacturing

## ABSTRACT

Commercial Li-ion cell electrodes comprise a random mix of the constituent materials largely unchanged for more than three decades. During fast charge/discharge, electrode-scale Li-ion concentration gradients develop, along with a spatially heterogeneous distribution of overpotential, utilization and degradation of active material, which ultimately restricts the range of realizable energy-power combinations. We expand energy-power characteristics and reduce cell degradation rate using electrodes that are compositionally graded at the microscale to homogenize active material utilization. Trapezoidal-graded composition LiFePO<sub>4</sub> cathodes, enabled by a layer-by-layer deposition technique, are compared with conventional electrodes: at an energy density of 500 Wh L<sup>-1</sup> the best graded electrode design increased power density from approximately 100 W L<sup>-1</sup> to 630 W L<sup>-1</sup>, while at a power density of 300 W L<sup>-1</sup>, the energy density increased from approximately 420 Wh L<sup>-1</sup> to 600 Wh L<sup>-1</sup>. The results highlight the potential for new manufacturing approaches and electrode designs to provide performance enhancements for existing and future Li ion battery chemistries.

## 1. Introduction

To meet the performance demands of energy storage applications in

electric vehicles (EVs) there is a need for improved Li-ion batteries (LIBs) that combine high energy density with improved power density, slower capacity degradation and reducing cost [1–3]. Existing commercial LIBs

\* Corresponding author. Warwick Manufacturing Group, University of Warwick, Coventry CV4 7AL, UK.

E-mail address: [Chuan.Cheng@warwick.ac.uk](mailto:Chuan.Cheng@warwick.ac.uk) (C. Cheng).

<https://doi.org/10.1016/j.jpowsour.2022.231758>

Received 20 December 2021; Received in revised form 3 June 2022; Accepted 14 June 2022

Available online 23 June 2022

0378-7753/© 2022 The Authors. Published by Elsevier B.V. This is an open access article under the CC BY license (<http://creativecommons.org/licenses/by/4.0/>).

trade energy density for power density (and vice versa), and the performance window for both high power and high energy density is comparatively restricted [4]. Most effort on widening LIB energy-power performance has concerned the formulation of novel battery chemistries with intrinsically fast Li-ion diffusion and high energy density [5,6]. While steady progress has been made in LIB energy density (and huge progress in cost reduction), a step-change in LIB power-energy performance via a new electrochemically active material may be achievable only at increased cost [7]. Meanwhile, time is running out to meet carbon neutral commitments, e.g. 2050 in the UK and the EU, and advances in energy storage performance must be accelerated [8].

The energy-power density trade-off in LIBs applies to all negative and positive electrodes and their combination because it is a consequence of the way batteries are constructed, in particular the electrode microstructure [9]. Electrochemical reaction kinetics are generally faster than the mass transport of Li-ions in either solid active particles or in the liquid electrolyte [10,11]. Consequently, at all but the very slowest charge/discharge rates, the diffusion control of electrochemical processes leads to a heterogeneous spatial distribution of the Li ion concentration and state-of-charge (SOC), most strongly through the electrode thickness [12–16]. Although the movement of Li ions in the electrolyte is generally tortuous because of the complex, inter-connected pore structure, the net ionic flux is principally through thickness and, for example, typically leads to Li-ion enrichment close to the separator and depletion close to the current collector for a positive electrode during discharging [17,18]. At increased C-rates, i.e. to sustain a high reaction current, regions of low Li-ion concentration will lead to a local increase in diffusion overpotential and contributes to the total charge-transfer overpotential in Butler-Volmer reaction kinetics [19,20]. As a result, the cut-off voltage for charge or discharge is reached within a much shorter period than at lower C-rates, and local insertion/de-insertion reactions from active materials are incomplete [18,21]. Consequently, only a fraction of the available capacity is achieved at fast rates [12,17,22]. A further consequence of overpotential heterogeneity is that some regions of the electrode are “over-charged”, which leads to unnecessary particle pulverisation [13,21] and capacity fade, or even the well-known case of local Li plating in graphite-based negative electrodes [23].

Commercially, electrodes are optimized towards high energy or high power characteristics [24]: high energy cells use thicker electrodes and/or a higher active material weight fraction to reduce the number of current collectors and separators, but sacrificing power density [4]; high power cells use thinner electrodes, and/or smaller sized active particles, higher porosity, and/or more carbon additives, but with a sacrifice in energy density [24,25].

Compared with the exploration of new LIB chemistries, the design of more favourable electrode structures has received only recent attention [26], partly due to a lack of manufacturing flexibility. Currently, almost all LIB electrodes are manufactured by mixing the active material, carbon conductive additives and a polymeric binder in a liquid that suspends the actives and additives and dissolves the binder [9]. The mixture is continuously coated onto metal foil current collectors through a slot-die followed by evaporation of the carrier/solvent liquid and calendaring [9]. This process has been developed spectacularly to the giga-factory scale (typically 20–40 GWh production per year) [27]. From a microstructural point of view, the objective of manufacture is to produce an identical, essentially random mixture of the constituents through the electrode thickness and within the plane (over many 100's of m<sup>2</sup>), uniformly well-adhered to the foil. As installed capacity continues to ramp up, there is inertia to explore other manufacturing approaches that might offer more microstructural control but where the cost-benefits are not clear or sufficiently advantageous. For example, the benefits of aligning electrode porosity in the through thickness direction have been shown by simulation and experiment for many years, but a competitive, productive route for manufacture remains elusive, and engineered porosity (for example by sacrificial pore templating) usually increases pore fraction and undermines volumetric performance

[28–30].

There remains controversy of the benefits – and under what conditions – of graded microstructure electrodes in which local particle size, fractions of materials, or type of material deliberately varies place to place [31–34]. At very slow charge rates, the cell is close to equilibrium conditions, and capacity only controlled by thermodynamic considerations such as the total amount of electrochemically active material and its intrinsic capacity. Graded electrodes should not offer any benefit under these conditions, and only when dynamic or kinetic effects become important might microstructural influence become apparent.

In general, simulation has been a more convenient approach to explore the dynamics of graded electrodes because processes that control microstructure point-to-point during manufacture have not been available until recently [34–37]. Where grading has been investigated experimentally, there has been difficulty in fabricating electrodes that offer a fair comparison of graded versus conventional electrodes. For example, when active particle diameter is graded through-thickness, the local porosity fraction also tends to vary so that similar weight electrodes have different thicknesses. This type of interdependency makes it difficult to unpick experimentally the underlying benefits – or deficiencies – of graded electrodes and microstructural design.

Previous experimental work on graded electrodes has included local pore fraction or particle size grading [25,31,32,34,38], pore templating [28,29,39], and layered arrangements using multiple slurry casting/-drying/calendaring steps [37,40]. These studies have shown some benefits of grading under some configurational and charge/discharge conditions, as well as some practical challenges such as higher electric resistivity at layer interfaces [41], and inter-layer cracking during long-term cycling [42]. It was demonstrated experimentally for LiFePO<sub>4</sub> and Li<sub>4</sub>Ti<sub>5</sub>O<sub>12</sub> particles that if the local fraction of conducting carbon additive was increased close to the current collector, the C-rate performance was much better than uniformly distributed, random mixture electrodes [35,36], consistent with similar findings for multi-layered electrodes [43]. The improved performance was attributed to lower impedance and homogenization of local reactivity and overpotential, supported by modelling insights [44].

Overall, the literature suggests that grading, in some circumstances can be beneficial, but there is not a “universal” optimum, and any optimum will depend on the active material involved, electrode thickness and porosity, and performance metrics of interest. Indeed, for some electrode formulations a random, uniform mixture may be close to optimum, and only the relative fraction of each component is important.

We present the manufacture and comparative performance of various LIB positive electrodes with controlled local fractions of active material (LiFePO<sub>4</sub>, LFP), conductive carbon and binder through the electrode thickness. We select LFP because electrode performance is known to be sensitive to grading effects [35,36]; it also has a relatively low intrinsic capacity making optimization to sustain capacity performance valuable. We investigate active materials loadings of 90 wt% that are significantly higher than previous work [35,36]. The electrodes are additively manufactured by a layer-by-layer spray deposition technique, achieving through-thickness grading with near μm-scale resolution. Critically, we vary local composition while producing a range of electrodes with the same overall approximate weight, porosity, and proportion of materials. This level of compositional control, and the ability to use exactly the same materials used in the ubiquitous slurry casting electrode fabrication route allows detailed “back-to-back” comparison. While previous work considered only monotonic through-thickness grading arrangements, we explore designs that increase local carbon and binder (CAB) fractions in the region of the electrode lower (electrode/current collector) and upper (electrode/separator) interfaces, and maximize active fraction in electrode central regions – producing a “trapezoidal” or “flat top mountain” distribution of active material through the thickness (e.g. Fig. 1b). Higher binder fraction at the current collector may increase adhesive strength and mechanical stability while more carbon can reduce contact resistance [45]. The benefits of more

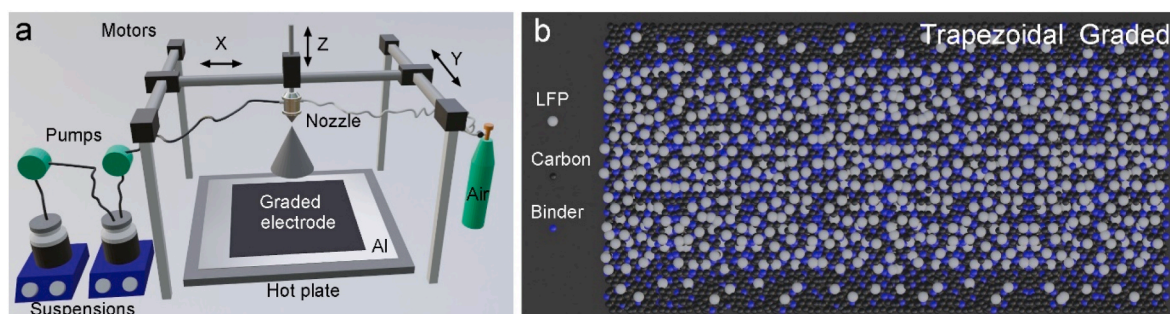


**Fig. 1.** (a) Schematic illustration of the experimental set-up for the fabrication of composition graded LIB electrodes. (b) Schematic depiction of a trapezoidal-graded active materials, carbon and binder distribution through the electrode thickness.

CAB towards the separator are more speculative, and part of the hypothesis explored here. Benefits might include: (i) reducing the fraction of active material exposed to the highest local Li concentrations in the near-separator region and so helping to avoid excessive SEI formation or other degradation mechanisms [46,47], and (ii) increasing the local ionic mobility at the electrode-separator interface to facilitate ion transport and so prevent excessively steep gradients in bulk electrolyte concentration forming across the electrode [44]. Another feature of the graded arrangements is that for a constant overall CAB fraction as used here, relatively high local CAB fractions at the current collector and separator region must be balanced by a reduction in the CAB fraction in the electrode central region. In turn, this may reduce CAB blocking or shadowing of active particle surface in this region, which may help to promote higher achievable electrode capacities.

## 2. Experimental

### 2.1. Graded electrode fabrication

A layer-by-layer, additive manufacture spray deposition route for LIB electrodes has been developed (Fig. 1a) that fabricates A5 (148 mm × 210 mm) area double-sided electrodes for pouch cells [48–51]. The process operates with conventional electrode slurries and compositions but with a greater dilution to enable atomization into a spray that deposits on a current collector foil. During spraying, a peristaltic pump controls the flow rate of suspension to the spray head where it is atomized using compressed air. The arising cone-shaped spray plume is scanned cyclically under computer control over a foil current collector in zig-zag pattern using a x-y-z manipulator gantry. The foil is attached to a heated vacuum chuck held at 140 °C to promote near-instant drying of the droplets and evaporation of the solvent on deposition. There is no significant re-suspension of previously deposited and dried layers, so the

**Table 1**

Materials and formulations used to produce graded, trapezoid-shaped through thickness compositional variations. The overall weight ratio of LFP active material: carbon:binder was 90:5:5 (wt.%) for Trapezoid 1 to 4 and Uniform-90, and 80:10:10 (wt.%) for Uniform-80 electrode. To fabricate each electrode, a total of 3 g solid materials was sprayed onto the current collector under otherwise identical conditions.

Electrode	Suspension A					Suspension B					Suspension C				
	AM (mg)	Carbon (mg)	Binder (mg)	NMP (mL)	IPA (mL)	AM (mg)	Carbon (mg)	Binder (mg)	NMP (mL)	IPA (mL)	AM (mg)	Carbon (mg)	Binder (mg)	NMP (mL)	IPA (mL)
Trapezoid-1	405.0	15.3	15.3	5	95	405.0	63.6	63.6	5	95	1890.0	71.1	71.1	10	190
wt.% (overall)	13.50 (93.0)	0.51 (3.5)	0.51 (3.5)			13.50 (76.0)	2.12 (12.0)	2.12 (12.0)			63.0 (93.0)	2.37 (3.5)	2.37 (3.5)		
wt.% (local)															
Trapezoid-2	648.0	24.3	24.3	5	95	162.0	54.6	54.6	5	95	1890.0	71.1	71.1	10	190
wt.% (overall)	21.60 (93.0)	0.81 (3.5)	0.81 (3.5)			5.40 (59.8)	1.82 (20.1)	1.82 (20.1)			63.0 (93.0)	2.37 (3.5)	2.37 (3.5)		
wt.% (local)															
Trapezoid-3	648.0	17.1	17.1	5	95	162.0	83.1	83.1	5	95	1890.0	49.8	49.8	10	190
wt.% (overall)	21.60 (95.0)	0.57 (2.5)	0.57 (2.5)			5.40 (49.4)	2.77 (25.3)	2.77 (25.3)			63.00 (95.0)	1.66 (2.5)	1.66 (2.5)		
wt.% (local)															
Trapezoid-4	1080.0	28.5	28.5	5	95	270.0	86.1	86.1	5	95	1350.0	35.4	35.4	10	190
wt.% (overall)	36.00 (95.0)	0.95 (2.5)	0.95 (2.5)			9.00 (61.0)	2.87 (19.5)	2.87 (19.5)			45.00 (95.0)	1.18 (2.5)	1.18 (2.5)		
wt.% (local)															
Uniform-90											2700.0	150.0	150.0	10	190
wt.%											90.0	5.0	5.0		
Uniform-80											2400.0	300.0	300.0	10	190
wt.%											80.0	10.0	10.0		

instantaneous, local fraction of electrode components is “frozen” into the electrode structure. The principal benefit is the ability to change the spray composition over time, or to mix multiple sprays, allowing electrodes with through-thickness (or in-plane) variations in composition, particle size, binder fraction, discrete inter-layers, etc. to be fabricated reproducibly and relatively quickly.

Previous work showed the benefits of a simple, monotonically varying active material and carbon distribution in LFP-based electrodes [35], but here we investigate if any further benefit can arise for more complex trapezoid arrangements, shown schematically in Fig. 1b, i.e. the active fraction starts relatively low at the current collector (and the CAB fraction is correspondingly relatively high), increases with electrode thickness to a maximum plateau fraction, and then reduces again at the separator. Table 1 lists the electrode materials for each arrangement. All the graded electrodes had overall electrode active:carbon:binder compositions of 90:5:5 (wt.%), along with uniform electrodes of either 90:5:5 or 80:10:10. To ensure similar electrode thicknesses and areal loading, the total electrode mass sprayed and all other parameters (including electrode porosity (see later), moving velocity of the spray nozzle (20 mm s<sup>-1</sup>), distance between nozzle and substrate (150 mm), pressure of the compressed air (0.4 bar), temperature of the substrate (140 °C), pumping rate of the suspension (see below), etc.) for all electrodes were kept constant during fabrication.

To fabricate the trapezoidal active material distributions, three suspensions A, B and C were used (Table 1). Step 1: suspensions A and B were divided into two equal volume suspensions A1 and A2, and B1 and B2. Step 2: suspension A1 was pumped into suspension B1 at a rate of 2.25 mL min<sup>-1</sup> and suspension B1 was sprayed at 4.5 mL min<sup>-1</sup> onto the heated current collector via a nozzle (ViscoMist, Lechler GmbH, Germany). Because suspension A1 flowed into suspension B1, the fraction of electrode materials deposited gradually changed. Both suspensions were magnetically stirred throughout until both suspensions were exhausted. Step 3: suspension C was sprayed at 4.5 mL min<sup>-1</sup> until exhausted. Step 4 was the exact inverse of Step 2: suspension B1 was pumped into A1 at a rate of 2.25 mL min<sup>-1</sup> and A1 was simultaneously sprayed at 4.5 mL min<sup>-1</sup> until both were exhausted. A MATLAB® code was used to calculate the resulting, nominal through thickness local weight ratios [35].

All the suspension were based on LiFePO<sub>4</sub> with a particle size of ~300 nm (Hydro-Québec, Canada), Super-P carbon additive (MTI, USA), PVDF binder (polyvinylidene fluoride, Mw~534,000, Sigma-Aldrich), and a solvent mixture of 1-Methyl-2-pyrrolidinone, (≥99.0%, Sigma-Aldrich) and IPA (2-propanol, 99.5%, Sigma-Aldrich) at 1:9 vol ratio. Suspensions were prepared by ball milling of the materials and solvent at 300 rpm for 1 h (FRITSCH Pulverisette 6, Germany) followed by high energy probe ultrasonication for 2 h (20Hz and 750W, Vibra-cell, Sonics Inc., US).

## 2.2. Coin cell assembly

The areal materials loading of all the LFP cathodes, irrespective of the materials arrangement, was 15.4 ± 0.7 mg cm<sup>-2</sup>. Note these areal electrode loadings are significantly higher than most comparable studies that use 3–5 mg cm<sup>-2</sup> [52]. Higher loadings were chosen to amplify any differences between the arrangements, and because higher loadings are always more desirable so long as performance is not compromised.

The LFP cathodes were dried overnight at 60 °C and then calendared to similar porosities (55–56%), and punched disks of 12 mm diameter were obtained. For 90:5:5 graded and uniform electrodes, the calendared thicknesses were 104 ± 7 μm, electrode densities were 1.48 ± 0.04 g cm<sup>-3</sup>, and electrode porosities were 54.6 ± 1.4% (averaged from ~50 electrodes and typically 8 electrodes fabricated for each arrangement). Applying a *t*-test to these data, at a confidence level of 95%, the confidence interval for electrode thickness was ± 2.0 μm, for electrode density ± 0.024 g cm<sup>-3</sup>, and for porosity ± 0.74%. For the 80:10:10 uniform electrodes, the calendared thickness were 121 ± 2 μm,

electrode densities were 1.30 ± 0.02 g cm<sup>-3</sup>, and electrode porosities were 56.3 ± 0.7%. The electrode porosity *p* was calculated according to:

$$p = \left[ 1 - \rho \left( \frac{f_{AM}}{\rho_{AM}} + \frac{f_C}{\rho_C} + \frac{f_B}{\rho_B} \right) \right] \times 100\% \quad (1)$$

where  $\rho$  is the electrode density;  $f_{AM}$ ,  $f_C$ , and  $f_B$  are weight fractions of active materials, carbon and binder, respectively;  $\rho_{AM} = 3.6$  g cm<sup>-3</sup>,  $\rho_C = 1.8$  g cm<sup>-3</sup>, and  $\rho_B = 1.74$  g cm<sup>-3</sup> are the densities of active materials, carbon (super-P) and binder (PVDF), respectively. Although the electrodes with  $f_{AM} = 80\%$  had a lower calendared density than those with  $f_{AM} = 90\%$ , once the relative densities of the differing fractions were accounted for, the electrode porosities were all closely similar (55–56%) with an electrode materials loading of 15.4 ± 0.7 mg cm<sup>-2</sup>.

CR2032 half-cells were assembled with the LFP-based positive electrodes working against Li foil, a Celgard separator, and 1 M LiPF<sub>6</sub> in ethylene carbonate and dimethyl carbonate electrolyte (EC/DMC = 50/50 v/v, Sigma-Aldrich, UK) electrolyte. Before assembling, all cell components were stored in a vacuum oven at 70 °C inside an Ar filled glovebox for more than 5 h and assembled into cells within the same glovebox. As-assembled cells were aged for 6–12 h before testing.

## 2.3. Electrochemical testing

Coin cells were tested using a battery cycler (Arbin Instruments, USA, Models: BT-G-25 and IBT21084LC) in the potential range 2.5–4.2 V vs. Li/Li<sup>+</sup> for LFP half-cells at room temperature and at various C-rates from 0.1 to 7C. Here, 0.1C corresponded to 17.0 mA g<sup>-1</sup>. Within each cycle, charging and discharging were performed at the same C-rate.

## 2.4. Materials characterization

After electrode calendaring, pristine electrode cross-sections were observed in a Carl-Zeiss Merlin (Germany) high-resolution field emission scanning electron microscope (FE-SEM) combined with an Oxford Instruments (UK) Xmax 150 energy-dispersive X-ray spectroscopy (EDX) detector. EDX element mapping and line scanning across the electrode thickness were performed to obtain qualitative element distributions. Electrode cross-sections shown in Fig. 2 were prepared by breaking the electrodes with tweezers.

## 3. Results and discussion

The plots in Fig. 2a–d shows the ideal, designed local fraction variations as a function of distance from the electrode surface (close to the separator) “down” towards the current collector for the electrodes given in Table 1. All the electrodes had the same overall composition ratio of active material LFP:carbon:binder of 90:5:5 (wt.%), the same overall coating thickness and density, but with different local composition variations through the electrode thickness: a uniform distribution in Fig. 2a (U90 hereafter) and trapezoidal distributions 2, 3 and 4 in Fig. 2b, c and d (T2, T3, T4 hereafter). Superimposed solid symbols in Fig. 2a–d shows EDX line scan intensity data from spray printed electrode cross-sections for Fe Kα1, C, and F Kα1 that depict the distribution of LFP, carbon conductive additive and PVDF binder, respectively. The EDX intensity data cannot be interpreted directly as the local weight fraction of each of the materials. Nonetheless the EDX traces provided reassurance that experimental distributions qualitatively matched and differentiated the uniform (Fig. 2a) and the trapezoidal designs (Fig. 2b–d). For example, the increased thickness of the carbon and binder rich region at the electrode periphery from 15% of total thickness in T3 (Fig. 2c) to 25% in T4 (Fig. 2d) was clearly differentiated. As intended, the electrode thicknesses were almost identical.

Fig. 2e–h shows EDX element maps superimposed on the SEM images (shown in Fig. S1 of the Supplementary Data) of the uniform and graded electrodes cross-section corresponding to the designs in Fig. 2a–d,



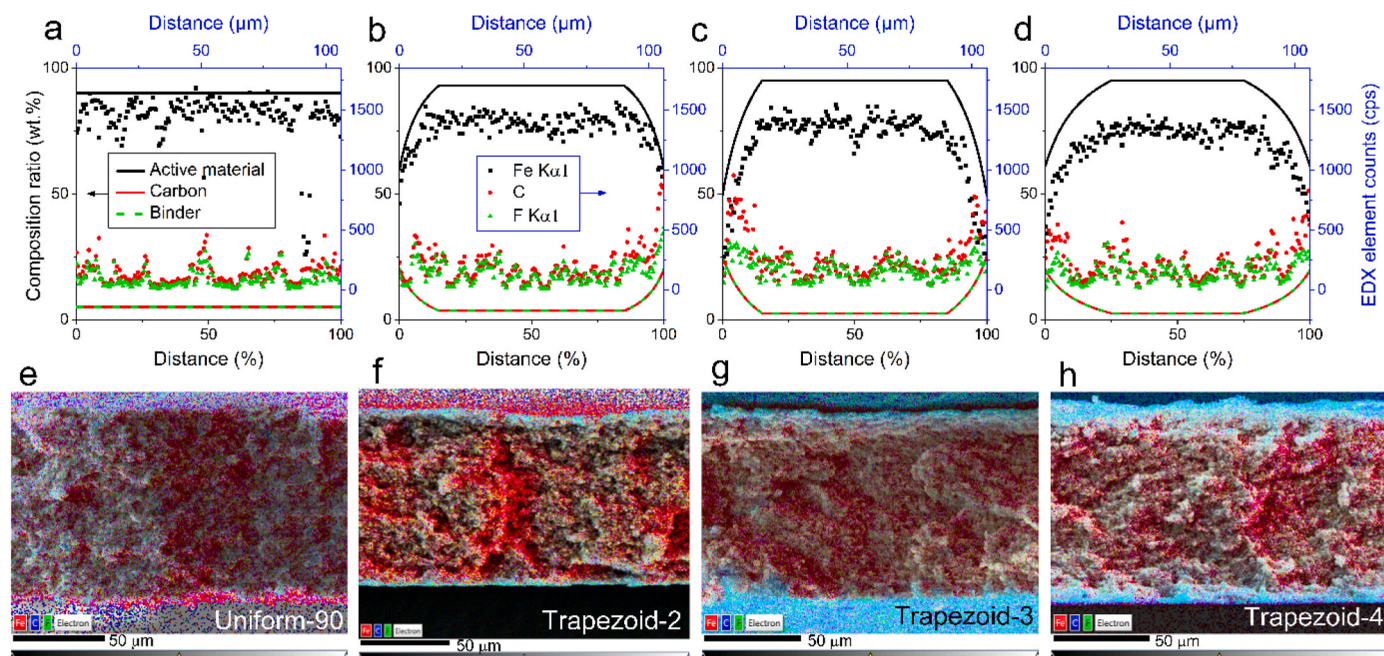


**Fig. 2.** (a–d) Graded electrodes with a trapezoidal profile of active material (LFP), with corresponding local variations in carbon and binder fraction, as a function of distance from the separator, through thickness towards the current collector. Solid lines represent the idealised, designed distribution; solid symbols represent the measured, approximate materials distribution according to energy-dispersive X-ray spectroscopy (EDX) through-thickness line scans. (e–h) EDX element maps of the electrode cross-sections corresponding to (a–d), respectively. Fe (red) depicts active material LFP, C (blue) depicts conductive additive, and F (green) depicts PVDF binder. All electrodes have the same average composition ratio of LFP:carbon:binder of 90:5:5 (wt.%). Fabrication conditions are given in Table 1. (For interpretation of the references to colour in this figure legend, the reader is referred to the Web version of this article.)

respectively. The micrographs and maps show there were no step changes in local composition and no internal delamination.

For ease of comparison, Fig. 3a shows the electrode materials design for U90 and the graded electrodes T1, T2 and T3 (Table 1) in a single plot. The relative thickness of the central plateau of high LFP fraction was maintained at 70% of the total thickness, but the graded regions differed. For example, in the plateau region, T1 and T2 had the same composition ratio of 93:3.5:3.5 (wt.%) and T3 had a ratio of 95:2.5:2.5, but at the edges of the graded region the ratios were 76:12:12 for T1, 59.8:20.1:20.1 for T2, and 49.4:25.3:25.3 for T3.

Fig. 3b shows that at low C-rate (0.1C) the electrodes had similar discharge capacities of  $\sim 147 \text{ mAh g}^{-1}$  and microstructural design played no differentiating role. As the C-rate increased up to 3C, all the electrodes had reduced capacity, which should be expected, particularly given relatively high electrode thicknesses of  $\sim 100 \mu\text{m}$  after calendaring. Electrode T3, with the highest CAB fraction and lowest active

fraction at the periphery but the highest active fraction in the plateau region, retained the highest capacity of  $\sim 3$  times the uniform counterpart at 1C. All the electrodes had similar degradation rates during cycling at 0.5C (Fig. 3c), but the improved capacity retention of the graded electrodes compared with the uniform electrode was maintained. These data suggest that electrode capacity was sensitive to the micro-arrangement of constituents: the C-rate performance was improved by redistributing CAB to the electrode upper and lower regions, with a consequent increase in active material fraction in central regions.

Galvanostatic charge-discharge curves for U90, T1, T2 and T3 electrodes are plotted in Fig. 4a–d respectively. The ability to maintain capacity with increasing rate C-rate from 0.1C to 1C was confirmed as  $\text{U90} < \text{T1} < \text{T2} < \text{T3}$  with discharge capacities at 1C of 43, 62, 89 and 120  $\text{mAh g}^{-1}$ , respectively. The corresponding first derivative of capacity to voltage ( $dQ/dE$ ) for each electrode is plotted as a function of voltage in Fig. 4e–h. The peak of  $dQ/dE$  identifies the voltage position of the redox

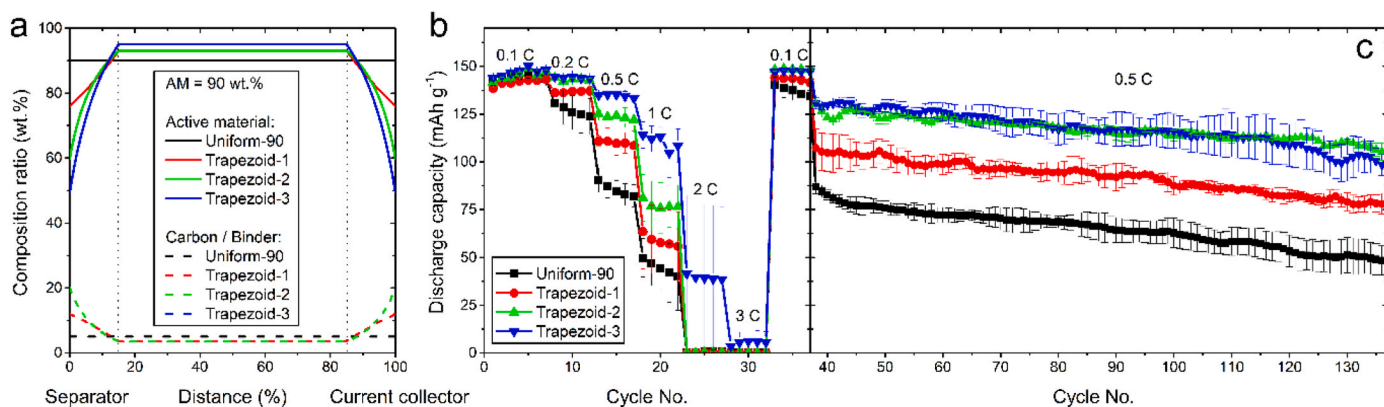


**Fig. 3.** C-rate and cycling performance of LFP-half cells with trapezoidal graded and uniform cathodes. (a) The designed through-thickness materials distribution. (b) Specific discharge capacity at different C-rates. (c) Cycling performance at 0.5C over 100 cycles, tested immediately after the C-rate testing in (b). All electrodes had the same overall composition ratio of active material:carbon:binder of 90:5:5 (wt.%).

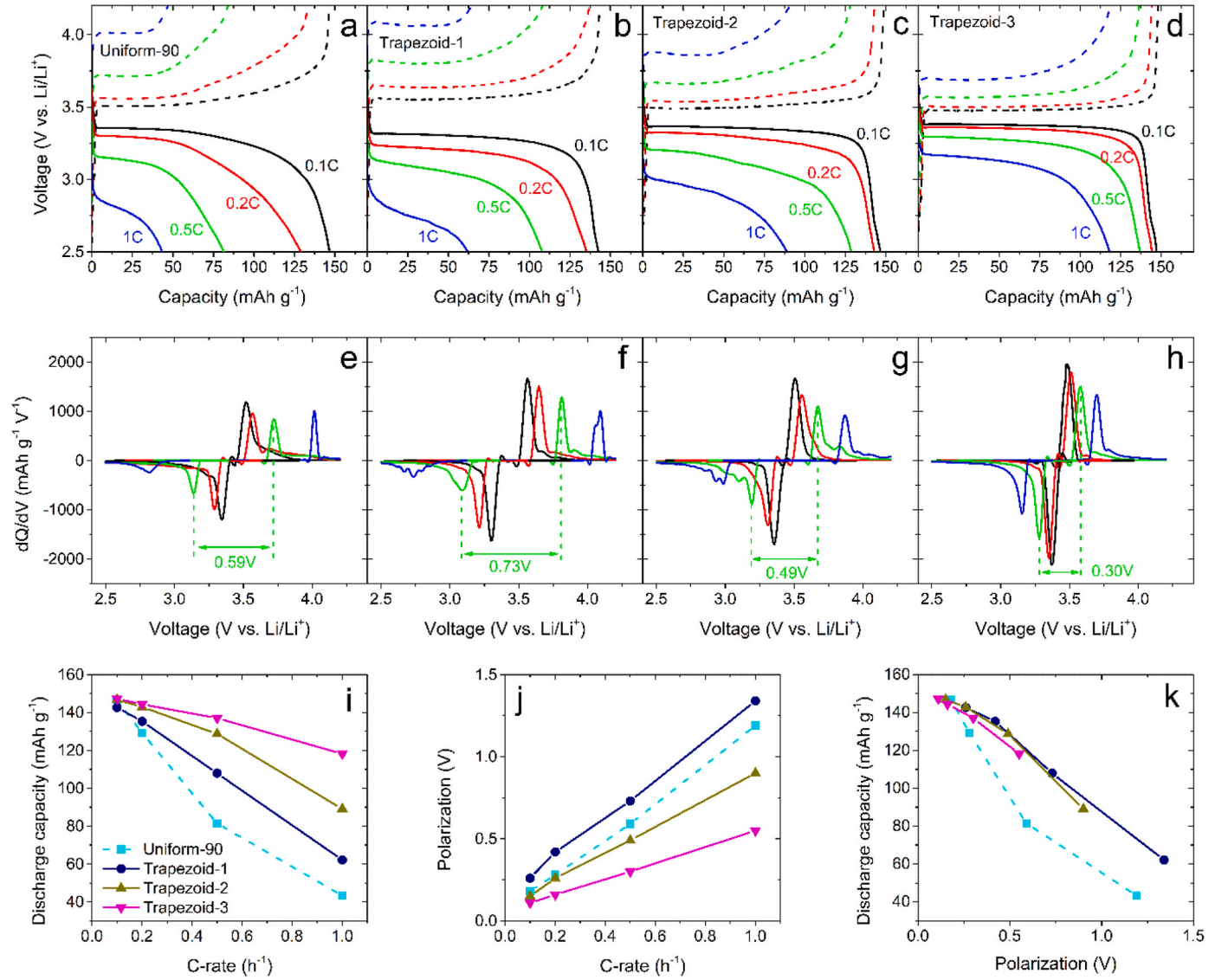


**Fig. 4.** (a–d) Galvanostatic charge-discharge curves of the LFP half-cells with U90, T1, T2, and T3 cathodes, respectively. (e–h) First derivative of capacity with respect to voltage ( $dQ/dE$ ) against voltage, corresponding to (a–d). (i) Discharge capacity as a function of C-rate. (j) Polarization obtained from the voltage difference between galvanostatic charge and discharge curves as a function of C-rate. (k) Discharge capacity as a function of polarization.

reactions of Li-ion intercalation/deintercalation. With increasing C-rate, both anodic and cathodic peak voltages shifted from the open-circuit-voltage of  $\sim 3.43$  V, arising from a change in the associated overpotential  $\eta$ .

In the widely used Newman model of Li ion batteries [53], the Butler-Volmer equation is used to describe the reaction kinetics at the active particle/electrolyte interface.

$$i_n = i_0 \left[ \exp\left(\frac{\alpha_a F}{RT} \eta\right) - \exp\left(-\frac{\alpha_c F}{RT} \eta\right) \right] \quad (2a)$$

$$i_0 = F(k_a)^{\alpha_c} (k_c)^{\alpha_a} (c_{s,max} - c_s)^{\alpha_c} (c_s)^{\alpha_a} (c_e)^{\alpha_a} \quad (2b)$$

$$\eta = \Phi_s - \Phi_e - U(c_s) \quad (2c)$$

where  $i_n$  is the current density normal to the surface of active material due to the Li intercalation/deintercalation,  $i_0$  is the exchange current density,  $\alpha_a$  and  $\alpha_c$  are transfer coefficients of anodic and cathodic directions of a reaction,  $k_a$  and  $k_c$  are rate constants for the anodic and cathodic directions of the reaction,  $\eta$  is the local value of surface overpotential,  $\Phi_s$  and  $\Phi_e$  are electric potentials of solid phase and the liquid

(electrolyte) phase,  $c_e$  and  $c_s$  are the Li<sup>+</sup> concentrations in the electrolyte and the active material at the interface,  $c_{s,max}$  is the maximum Li<sup>+</sup> concentration in the active material, and  $U(c_s)$  is the open-circuit potential of active material that is  $c_s$  dependent. Eq. (2) shows the reaction rate strongly depends on the local overpotential ( $\eta$ ) and the local Li<sup>+</sup> concentrations in the active material ( $c_s$ ) and the electrolyte ( $c_e$ ) at the interface.

During discharge of a LFP cathode, Li<sup>+</sup> is intercalated first at the active particle surface and is then slowly transported through the particle according to Fick's 2nd law of diffusion [53].

$$\frac{\partial c_s}{\partial t} = \frac{1}{r^2} \frac{\partial}{\partial r} \left[ D_s r^2 \frac{\partial c_s}{\partial r} \right] \quad (\text{for } 0 < r < R_s) \quad (3a)$$

$$-D_s \frac{\partial c_s}{\partial r} = 0 \quad (\text{for } r = 0) \quad (3b)$$

$$-D_s \frac{\partial c_s}{\partial r} = \frac{i_n}{F} \quad (\text{for } r = R_s) \quad (3c)$$

The active particle was assumed to be spherical with a radius  $R_s$ .  $D_s$  is the diffusion coefficient of Li in the active particle. In Eq. (3c), the rate of

$\text{Li}^+$  ion transport at the particle surface corresponds to the rate of Butler-Volmer reaction kinetics. At fast C-rates, the vacancies at the particle surface to host  $\text{Li}^+$  may be saturated before Li vacancies beneath the surface are fully occupied, i.e.  $c_s \rightarrow c_{s,\max}$ , at the particle surface, and  $c_s \ll c_{s,\max}$  at the particle core. From Eq. (2b), the exchange current density ( $i_0$ ) tends to zero because  $c_s \rightarrow c_{s,\max}$ , at the particle surface. From Eq. (2a), in order to maintain the high current output at fast C-rates, the overpotential  $\eta$  has to be elevated to provide a larger driving force for the reaction to take place. As a result, the cell cut-off voltage will be reached within a relatively short time, before vacancies inside the particle are fully occupied by  $\text{Li}^+$ . This situation can be regarded as microscopic heterogeneity.

When all the active particles are now considered across the electrode thickness, macroscopic heterogeneity at the electrode level arises due to the inhomogeneous  $\text{Li}^+$  concentration in the electrolyte, which follows the moderately concentrated electrolyte theory [53,54].

$$\varepsilon \frac{\partial c_e}{\partial t} = \frac{\partial}{\partial x} \left[ D_e^{\text{eff}} \frac{\partial c_e}{\partial x} \right] + \frac{a(1 - t_0^+) i_n}{F} \quad (4a)$$

$$D_e^{\text{eff}} = D_e \varepsilon^b \quad (4b)$$

where  $x$  is along the electrode (and the cell) thickness,  $\varepsilon$  is electrode porosity,  $a$  is specific interfacial area of the electrode,  $t_0^+$  is transference number of  $\text{Li}^+$  in electrolyte,  $D_e^{\text{eff}}$  is the effective diffusion coefficient of the electrolyte,  $D_e$  is the intrinsic diffusion coefficient of the electrolyte, and  $b$  is the Bruggeman coefficient. According to numerical solutions of Newman's model [54],  $c_e$  reduces steadily from the electrode/separator interface to the electrode/current collector interface during discharging of a cathode, and this concentration gradient becomes steeper with increasing C-rate.

Under these conditions, for particles located close to the current collector of the cathode, the relatively low local  $c_e$  leads to reduced  $i_0$  according to Eq. (2b). The local reaction rate will be consequently reduced and there is not enough  $\text{Li}^+$  in the electrolyte to intercalate fully into the active cathode particle. For particles located closer to the separator where  $c_e$  will be relatively high, the particles tend towards fully intercalated. Therefore, particles across the electrode thickness as a whole are not homogeneously utilized at electrode thickness scale. To address this inhomogeneity in active material utilization, recent simulations of compositionally graded electrodes predicted that the reaction rate could be homogenized by rearranging the electrode materials micro-distribution through the electrode thickness [44] and similar to the ideas explored experimentally here.

Here, we assume the voltage difference between matching anodic and cathodic peaks gives an indication of the polarization between Li-ion deintercalation (anodic) and intercalation (cathodic) reactions, which are marked by the dashed vertical green lines in Fig. 4e–h. This polarization is approximately twice the overpotential for either deintercalation or intercalation reactions for a given C-rate [55].

Fig. 4i summarizes the discharge capacity data in Fig. 4a–d; Fig. 4j summarizes the polarization data from Fig. 4e–h as a function of C-rate; and finally, Fig. 4k then combines the data to show the strong relationship between discharge capacity and extent of polarization. Graded electrodes with higher capacity retention had lower polarization at each C-rate, i.e. a lower overpotential for redox reactions. Note electrode U90 had a lower polarization than T1 electrode (Fig. 4j) but its C-rate performance was nonetheless inferior; U90 also had a faster capacity decay with increasing polarization. As overpotential increases, the rate of side reactions generally also increases, driving the thickening of the SEI layer that increases internal resistance and further elevates overpotential [35, 46]. Fig. 4k shows that in terms of discharge capacity as a function of polarization, the behaviour of graded electrodes was similar but distinctly superior to the uniform electrode.

Fig. S2 in the Supplementary Data and Table 1 gives details of the design and performance of a further T4 arrangement in which the high

fraction active material plateau was reduced from 70% of the overall electrode thickness to 50%, and consequently, the edge gradient was less steep. In terms of C-rate capacity retention and degradation rate, T4 was inferior to T3, emphasising the importance of a wide plateau region rich in the active material, and redistributing more CAB to the electrode edges.

In this study the local binder fraction scaled with the local carbon fraction as it was assumed necessary always to have sufficient binder to embed the carbon into a CAB mixture. However, the binder is electrochemically inert and wastes mass and volume, does not contribute to electronic conductivity and may obscure active surface to Li-ions. Although not pursued in this paper, the spray deposition route allows for full decoupling of local binder and carbon fractions, even as the active material fraction also changes, and could be investigated as a route to minimise the overall fraction of parasitic binder in the electrode.

To explore further the materials distribution effects, cyclic voltammetry was conducted and the resulting plots for U90, T2, T3 and T4 electrodes are shown in Fig. 5a–d respectively. As the scan rate increased from 0.05 to 0.09  $\text{mV s}^{-1}$  both anodic and cathodic peak currents of the uniform electrode were similar while the peak area tended to shrink, indicative of sluggish reaction kinetics and reducing active material utilization as seen in the earlier C-rate data (Fig. 4). T2 and T4 electrodes exhibited slightly higher peak currents than U90, and the peak areas expanded over the range 0.05–0.08  $\text{mV s}^{-1}$ . For electrode T3, both peak current and peak area increased with scan rate, and the difference between peak potentials widened, consistent with its higher capacity retention.

To compare Li-ion mobility in the different electrodes anodic and cathodic peak currents were plotted as a function of the square root of the scan rate, as shown in Fig. 5e and f. Assuming diffusion controlled reactions, the slope of a best-fit line to the Randles-Sevcik equation is proportional to the Li-ion diffusion coefficient [56–58]:

$$\text{slope} = \frac{i_p}{v^{1/2}} = 0.4463 \left( \frac{F^3}{RT} \right)^{1/2} C^* A D^{1/2} \propto D^{1/2} \quad (5)$$

where  $i_p$  is the peak current,  $v$  is the potential scan rate,  $F$  is the Faraday constant,  $R$  is the gas constant,  $T$  is absolute temperature,  $C^*$  is the initial Li-ion concentration,  $A$  is the electrochemical active surface area, i.e. the sum of the active particle/electrolyte interfacial area, and  $D = D_0 \varepsilon^b$  is the effective Li-ion diffusion coefficient for porous electrode, where  $b$  is the Bruggeman coefficient,  $\varepsilon$  is electrode porosity, and  $D_0$  is the diffusion coefficient without porosity [44].  $C^*$  and  $A$  were assumed constant for all electrodes. It has been suggested that when the LFP electrode thickness is  $> 20 \mu\text{m}$  (or the electrode loading  $> 4 \text{ mg cm}^{-2}$ ), the Li-ion diffusion coefficient describes the overall diffusivity of the electrode rather than diffusivity in the LFP particles [59–61]. Given an electrode thickness  $\sim 100 \mu\text{m}$  and electrode loading  $\sim 15 \text{ mg cm}^{-2}$ , the Li-ion diffusion coefficients estimated here were not the intrinsic diffusivity of Li in LFP particles but reflected the effective Li-ion diffusivity, integrated over both particulate and electrode length-scales. Recent work has shown that for LIBs,  $\text{Li}^+$  diffusion limitations in the electrolyte are the principal restriction to high energy retention at fast charging [10].

Fig. 5e shows that for electrodes T2 to T4 there was a linear dependence of  $i_p$  (anodic) on  $v^{1/2}$  at scan rates  $< 0.07 \text{ mV s}^{-1}$ . For electrode U90, there was no best-fit because the scan rates were too high for electrodes of this high mass loading and thickness functioning. Note that due to the sluggish ion diffusion at the fast rates, U90 did not show inflection points (current peaks) at 0.09  $\text{mV s}^{-1}$ . Instead, the maximum and minimum current obtained at the positive and negative potential ends are plotted in Fig. 5e and f to provide some indication of rate response, but no fitting to these data was performed. As shown in Fig. 5e, the slope (and therefore Li-ion mobility) increased from T4 ( $2.05 \text{ A g}^{-1} \text{ mV}^{-1/2} \text{ s}^{1/2}$ ) to T2 ( $0.341 \text{ A g}^{-1} \text{ mV}^{-1/2} \text{ s}^{1/2}$ ) and then T3 ( $0.640 \text{ A g}^{-1} \text{ mV}^{-1/2} \text{ s}^{1/2}$ ), and similar to the trend for the cathode peak current



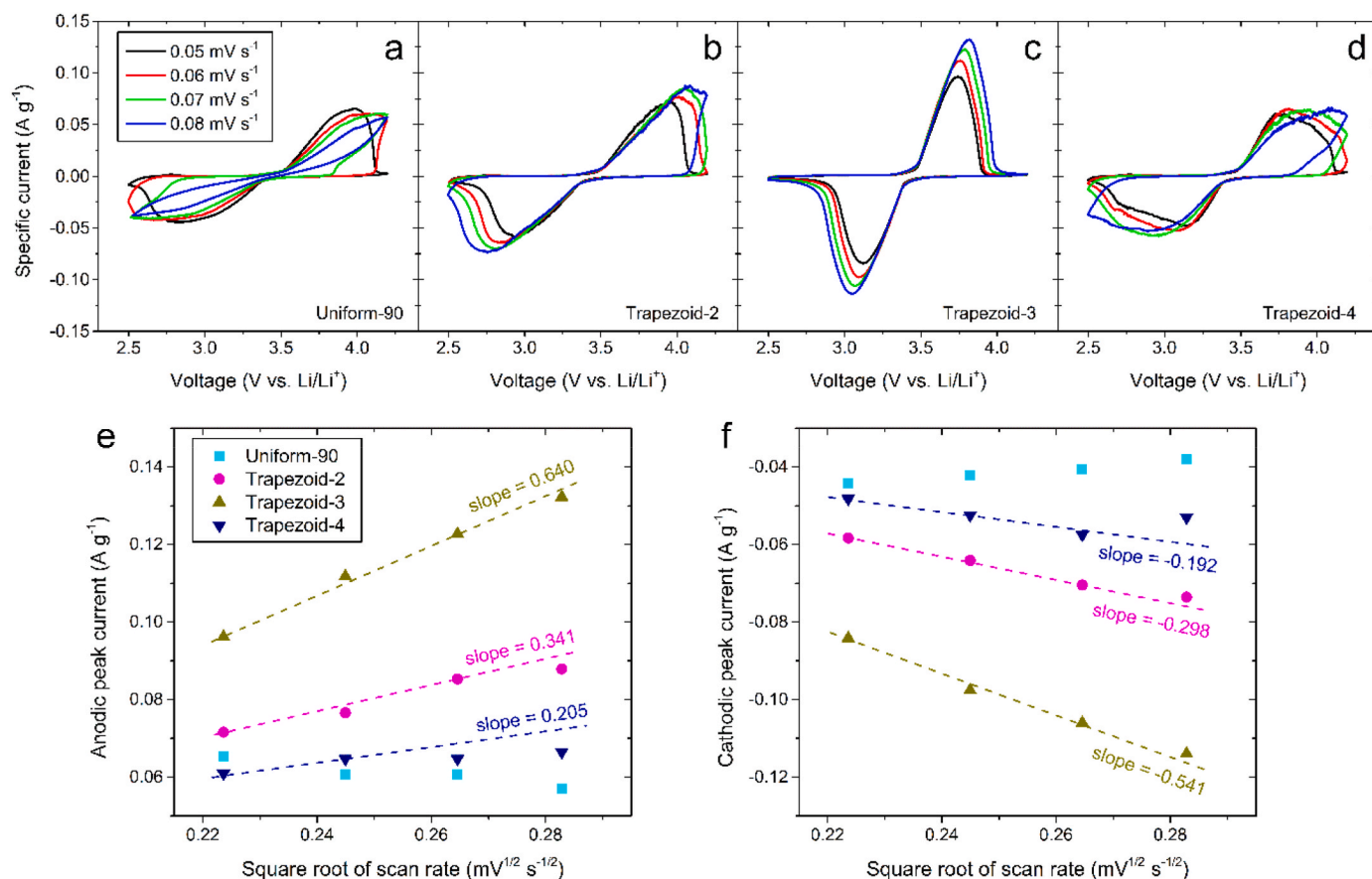


**Fig. 5.** Cyclic voltammetry of LFP half-cells with uniform and graded electrode configurations. (a) U90, (b) T2, (c) T3, and (d) T4. (e) Anodic peak current as a function of the square root of scan rate. (f) Cathodic peak current as a function of the square root of scan rate. All electrodes have the same overall composition ratio of active material:carbon:binder = 90:5:5 wt%.

shown in Fig. 5f.

Variations in pore fraction or tortuosity can have significant effects on Li-ion diffusivity throughout the electrode, but, to a first approximation, pore fraction was essentially the same for all the electrodes. Consequently, it is interesting to speculate on the reasons for the differing Li-ion diffusivity. Given that the aim of grading is to improve the spatial homogeneity of overpotential and local reaction current, it is consistent to infer that the apparent increasing diffusivity arose from more active material being utilized in the diffusion-limited energy storage reactions.

The best-performing T3 graded electrode with 5 wt% carbon and 5 wt% binder was compared with a conventional uniform electrode in which carbon and binder fraction were doubled to 10 wt% and the active fraction correspondingly decreased to 80 wt% (U80). A comparison of the carbon, binder and active distributions is shown in Fig. 6a. Usually, for electrodes of thickness  $\sim 100$   $\mu\text{m}$ , increasing the carbon fraction to 10 wt% would be expected to improve the C-rate response [62,63]; indeed, Fig. 6b and c confirm that U80 outperformed U90 in terms of capacity per unit weight of active material. The C-rate response of U80 was now similar to T3 up to 1C, although T3 maintained its superior capacity at 2C and 3C. In terms of capacity degradation during cycling at 0.5C, U80 was more similar to T3 than to U90, although T3 was again superior to both uniform electrodes. Fig. 6e and f shows the same gravimetric data replotted using the total electrode materials mass (active + carbon + binder). At 0.1C, the extra carbon in U80 provided little benefit and undermined gravimetric capacity, and thereafter, the C-rate response and degradation rate were now markedly inferior to T3. For example, T3 specific capacities were 133  $\text{mAh g}^{-1}$  (0.1C) and 102  $\text{mAh g}^{-1}$  (1C), while U80 capacities were 118  $\text{mAh g}^{-1}$  (0.1C) and 83

$\text{mAh g}^{-1}$  (1C); the T3 average degradation rate was 0.34  $\text{mAh g}^{-1}$  per cycle while for U80 it was 0.50  $\text{mAh g}^{-1}$  per cycle.

Although the response of the trapezoidal graded electrodes in Fig. 6e and f is significantly better than uniform electrodes, the response should also be considered in terms of linear graded arrangements that were the focus of previous work [35,36]. At a lower, less useful active fraction of 80 wt% LFP, the previous studies showed that linear grading (carbon-rich at the current collector for LFP electrodes) was superior to trapezoidal grading in terms of capacity with increasing C-rate. However, trapezoidal grading gave the slowest capacity degradation rate of all the electrodes studied during long term cycling. Therefore, combining prior and current work, the following trends can be seen: (i) linear and trapezoidal graded electrodes outperform uniform LFP-based electrodes in all principal figures of merit; (ii) linear grading from a carbon-rich current collector region produces the best dynamic response of electrode capacity to increasing C-rate; and (iii) trapezoidal grading sustains electrode capacity most effectively in long term cycling, consistent with our original hypothesis.

It should be emphasised that local variations in electrode composition will change the local electronic conductivity, ionic conductivity, diffusivity, etc, which in turn will change the overpotential distribution (and its various ionic and electronic contributions), and therefore local reaction rates. The best performing electrodes here, for a given C-rate, in effect represent the best balance of both local ionic and electronic limitations on the electrochemical response, integrated over the electrode thickness. These aspects are explored in further detail by impedance simulations elsewhere [44].

Fig. 7 shows the gravimetric/volumetric power density against energy density for LFP-based half-cells with various uniform and graded



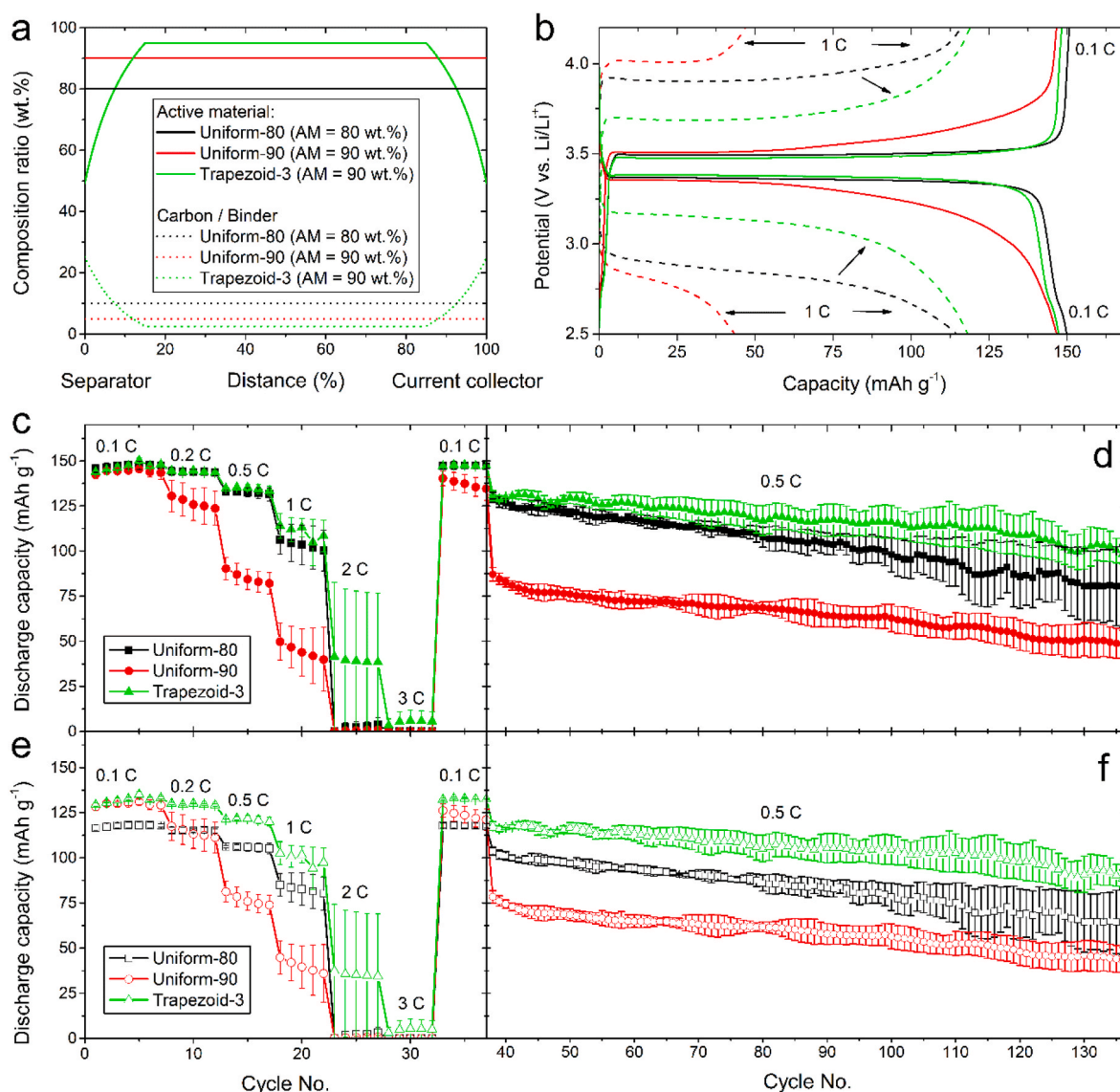


**Fig. 6.** Specific capacity comparison of optimized graded electrodes with uniform electrodes by considering active material mass only and whole electrode mass. (a) Schematic representation of the material distribution through the electrode thickness. Uniform-80 (U80) had composition ratio 80:10:10 (wt.%); Uniform-90 (U90) and Trapezoid-3 (T3) had composition ratio 90:5:5 (wt.%). (b) Galvanostatic charge-discharge curves of the various LFP half-cells at 0.1 and 1C. (c, d) Specific discharge capacity at different C-rates, and subsequent long-term cycling at 0.5C, when only the active materials mass was considered. (e, f) Specific discharge capacity re-calculated from (c, d) when considering the whole electrode materials mass (active material + carbon + binder).

electrodes. For electrodes with a composition ratio of 90:5:5 (wt.%), the gravimetric power versus energy performance could be ranked as  $\text{U90} < \text{T1} \sim \text{T4} < \text{T2} < \text{T3}$  (Fig. 7a). As seen before, at low C-rate all electrodes had similar energy density; with increasing C-rate, the materials distribution played an increasing differentiating role in power versus energy performance. For example, at the same power density of  $250 \text{ W kg}^{-1}$  ( $\sim 0.5\text{C}$ ), the energy density increased from  $243 \text{ Wh kg}^{-1}$  for U90 to  $473 \text{ Wh kg}^{-1}$  to T3 i.e. an increase of nearly 100%. Among graded electrodes, power versus energy performance was sensitive to the materials distribution (Fig. S2 further compares T4 and T3). U80 had a power-energy curve that sat between T2 and T3 when only active material mass was considered in the power/energy density calculation (Fig. 7a, pink line/symbols); however, when the whole electrode mass was considered, the U80 energy density reduced faster with increasing power than all the other electrodes due to the higher inactive material content (Fig. 7b, pink line/symbols). In terms of volumetric power density versus energy density in Fig. 7c, the power-energy curve for U80 shifted to the left in comparison with the graded electrodes (to lower energy densities),

principally due to its lower electrode density at a similar porosity as other electrodes, as described in the Experimental section.

In balancing power and energy densities for a uniform electrodes, increasing the carbon content from 5 wt% (U90) to 10 wt% (U80) is usually expected to increase the power significantly and reduce energy density, as confirmed by comparing black and pink curves above 0.2C in Fig. 7a–c, but sacrificing energy density at 0.1C by 10% (gravimetric, Figs. 7b) and 17% (volumetric, Fig. 7c).

In understanding the uniform versus graded performance, U80 may be considered a power-oriented formulation (higher carbon content) and U90 as an energy-oriented formulation (higher active material content). Graded formulations T1 to T3 are closer to energy-oriented because they have 90 wt% active material. However, graded electrode T3 has energy and power densities that are both significantly larger than the power-oriented electrode U80 i.e. blue versus pink in Fig. 7b and c and also highlighted in Fig. 7d. For example, at the same energy density of  $500 \text{ Wh L}^{-1}$ , the power density increases from  $\sim 100 \text{ W L}^{-1}$  (U80) to  $\sim 630 \text{ W L}^{-1}$  (T3) whereas at the same power density of  $300 \text{ W L}^{-1}$ , the

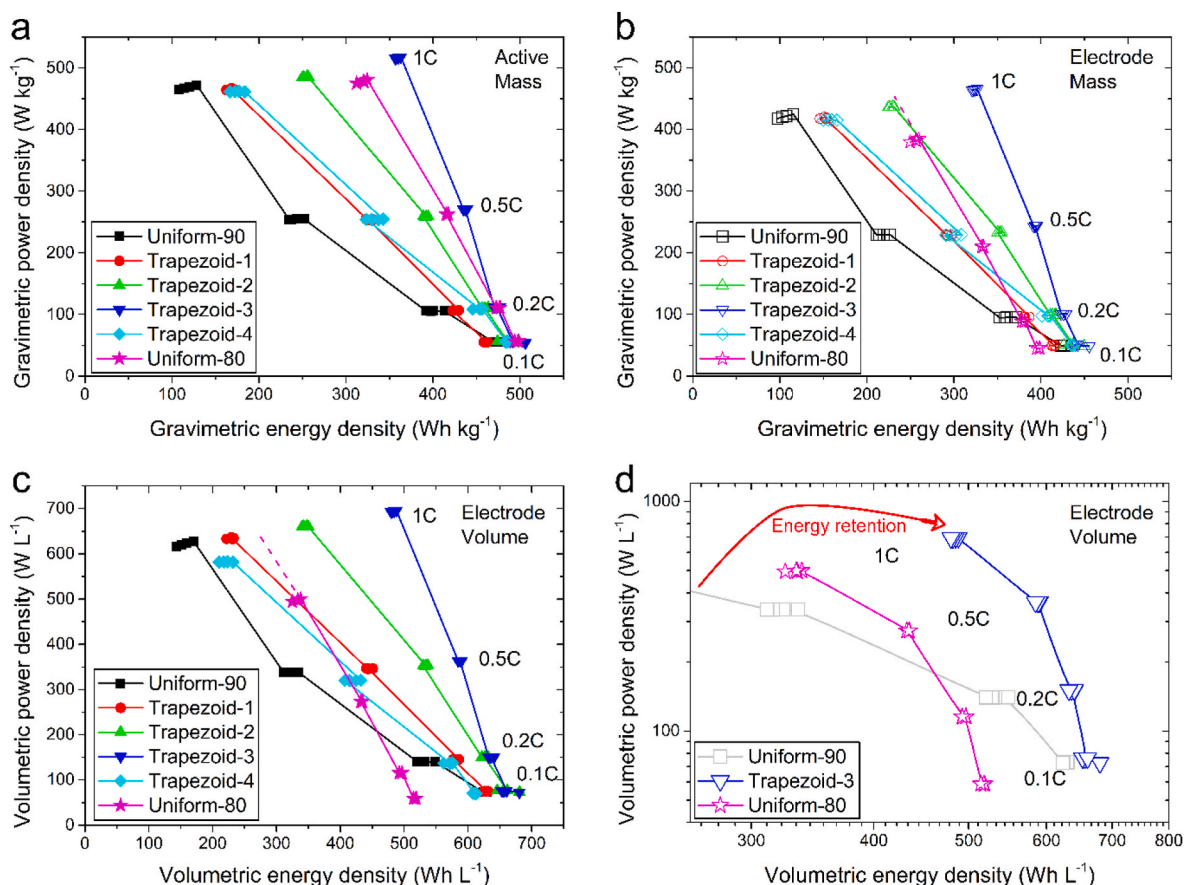


**Fig. 7.** Power density versus energy density for LiFePO<sub>4</sub>-based half-cells with various electrode configurations. (a) Gravimetric power density versus energy density when only the active material mass was considered; (b) Gravimetric power density versus energy density when the whole electrode materials mass (active material + carbon + binder) was considered; and (c, d) Volumetric power density versus volumetric energy density at the electrode level.

energy density increases from  $\sim 420 \text{ Wh L}^{-1}$  (U80) to  $\sim 600 \text{ Wh L}^{-1}$  (T3). This is achieved by reduced polarization (Fig. 4j) and consequently increased reaction currents that more efficiently utilizes the active materials as power demand (C-rate) increases.

Recent modelling work suggests that LFP might be particularly sensitive to carbon and/or CAB grading in electrodes [44] because LFP has a relatively low intrinsic electronic conductivity ( $\sim 10^{-9} \text{ S cm}^{-1}$ ) [64], although conductivity can vary depending on the extent of reduction/oxidation and the presence and effectiveness of any carbon coating. The results here confirm LFP electrodes can benefit from more precision in the CAB placement, and in comparison to previous work, the grading performance improvements are more compelling and achieved at a higher, practical active material loading of 90 wt% and in relatively thick electrodes. Further, while the most significant effect of carbon redistribution may be to reduce interfacial resistance that can be problematic in LFP-based electrodes [44], the results here show that energy storage behaviour is surprisingly responsive to the particular detail of this redistribution i.e. the range of graded electrode responses is diverse.

Other active materials with higher intrinsic electrical conductivity than LFP may not benefit from CAB redistribution as strongly, or may only show worthwhile grading sensitivity under high C-rate conditions and/or for relatively thick electrodes. However, we note that significant grading benefits for Li<sub>4</sub>Ti<sub>5</sub>O<sub>12</sub>-based anodes have been shown where similar constant thickness/loading comparisons have been made [36]. Further, by combining linearly graded LFP-based positive electrodes with LTO-based negatives electrodes in a full cell arrangement significant C-rate and cycling performance improvement were realized, along with new power-energy combinations unavailable with uniform electrodes [36]. Finally, the trapezoidal shapes explored here may still be

sub-optimal for LFP (or any active material), and both simpler or more complex variations can be conceived – layer by layer fabrication opens a very large electrode design space. Given the possibilities, trial and error exploration of this design space is impractical, and highlights the increasing importance of a model-guided electrode design methodology [44].

Although in this study overall electrode porosity was constant for all the electrode arrangements, in terms of a generic, flexible approach to electrode design, a potentially confounding factor is that local pore fraction – so far – cannot be independently controlled with the same accuracy as local binder, carbon and active material fraction. Although pore templates might be used to control pore fraction and tortuosity [30], templating is in general, difficult to scale whereas a benefit of the spray deposition, layer by layer approach is that it is readily scalable to larger areas.

#### 4. Conclusions

To advance understanding of the possible benefits of graded composition electrodes in LIB applications, we manufactured LiFePO<sub>4</sub>-based electrodes in which the distribution of active materials, carbon and binder through an electrode thickness was controlled with approximately micron-scale precision. Critically, weight per unit area, overall porosity and overall ratio of all materials was kept constant, regardless of the micro-distribution of materials, allowing for a fair back-to-back comparison of electrochemical performance. In the graded electrodes, the local carbon and binder (CAB) fraction was smoothly increased towards the interface with the current collector and with the separator, with a proportionate decrease in the local active fraction; in

central regions of the electrode, the local active materials fraction was relatively high (>90 wt%) and the CAB fraction reduced. Different graded and uniform material distributions were explored, showing significant differences in electrochemical behaviour, particularly as C-rate was increased.

The best performing graded electrode with overall 90 wt% active material and ~100 µm thickness had a higher power density than a high-power uniform electrode with twice as much carbon (and binder), while simultaneously providing higher gravimetric and volumetric energy density.

The principal advantage of grading was to reduce overpotential compared with identical uniform electrodes, and both anodic and cathodic reaction currents were strongly enhanced, which was interpreted as better utilization of the available active materials at high rates, resulting in higher capacity retention under all conditions studied. The reduced overpotential and more uniform utilization supported a marked reduction in degradation rate during intermediate C-rate cycling.

### CRedit authorship contribution statement

**Chuan Cheng:** carried out electrode design, manufacturing, data analysis, and paper writing, discussed the data, revised the manuscript. **Ross Drummond:** discussed the electrode design and optimization, discussed the data. **Stephen R. Duncan:** discussed the data, and. **Patrick S. Grant:** discussed the data, and, revised the manuscript, supervised the project.

### Declaration of competing interest

The authors declare that they have no known competing financial interests or personal relationships that could have appeared to influence the work reported in this paper.

### Data availability

Data will be made available on request.

### Acknowledgments

This work was supported by the Faraday Institution project Nextrode (FIR015), the UK Engineering and Physical Sciences Research Council (EPSRC) grant EP/P005411/1, and with some capital equipment provided by the Henry Royce Institute through EPSRC grant EP/R010145/1. We would like to thank Hydro-Québec (Canada) for providing the LiFePO<sub>4</sub> cathode materials.

### Appendix A. Supplementary data

Supplementary data to this article can be found online at <https://doi.org/10.1016/j.jpowsour.2022.231758>.

### References

- [1] The Roadmap Report: towards 2040 - A Guide to Automotive Propulsion Technologies, Advanced Propulsion Centre UK, Coventry, UK.
- [2] X.-G. Yang, C.-Y. Wang, Understanding the trilemma of fast charging, energy density and cycle life of lithium-ion batteries, *J. Power Sources* 402 (2018) 489–498.
- [3] J. Deng, C. Bae, A. Denlinger, T. Miller, Electric vehicles batteries: requirements and challenges, *Joule* 4 (2020) 511–515.
- [4] A.M. Boyce, D.J. Cumming, C. Huang, S.P. Zankowski, P.S. Grant, D.J.L. Brett, P. R. Shearing, Design of scalable, next-generation thick electrodes: opportunities and challenges, *ACS Nano* (2021).
- [5] M. Weiss, R. Ruess, J. Kasnatscheew, Y. Levartovsky, N.R. Levy, P. Minnmann, L. Stolz, T. Waldmann, M. Wohlfahrt-Mehrens, D. Aurbach, M. Winter, Y. Ein-Eli, J. Janek, Fast charging of lithium-ion batteries: a review of materials aspects, *Adv. Energy Mater.* 11 (2021), 2101126.
- [6] S.T. Myung, F. Maglia, K.J. Park, C.S. Yoon, P. Lamp, S.J. Kim, Y.K. Sun, Nickel-rich layered cathode materials for automotive lithium-ion batteries: achievements and perspectives, *ACS Energy Lett.* 2 (2017) 196–223.
- [7] L. Mauler, F. Duffner, W.G. Zeier, J. Leker, Battery cost forecasting: a review of methods and results with an outlook to 2050, *Energy Environ. Sci.* 14 (2021) 4712–4739.
- [8] L. Rosa, D.L. Sanchez, M. Mazzotti, Assessment of carbon dioxide removal potential via BECCS in a carbon-neutral Europe, *Energy Environ. Sci.* 14 (2021) 3086–3097.
- [9] C.D. Reynolds, P.R. Slater, S.D. Hare, M.J.H. Simmons, E. Kendrick, A review of metrology in lithium-ion electrode coating processes, *Mater. Des.* 209 (2021), 109971.
- [10] C. Heubner, M. Schneider, A. Michaelis, Diffusion-limited C-rate: a fundamental principle quantifying the intrinsic limits of Li-ion batteries, *Adv. Energy Mater.* 10 (2020), 1902523.
- [11] M.J. Lain, E. Kendrick, Understanding the limitations of lithium ion batteries at high rates, *J. Power Sources* 493 (2021), 229690.
- [12] J. Liu, M. Kunz, K. Chen, N. Tamura, T.J. Richardson, Visualization of charge distribution in a lithium battery electrode, *J. Phys. Chem. Lett.* 1 (2010) 2120–2123.
- [13] Y. Yang, R. Xu, K. Zhang, S.-J. Lee, L. Mu, P. Liu, C.K. Waters, S. Spence, Z. Xu, C. Wei, D.J. Kautz, Q. Yuan, Y. Dong, Y.-S. Yu, X. Xiao, H.-K. Lee, P. Pianetta, P. Cloetens, J.-S. Lee, K. Zhao, F. Lin, Y. Liu, Quantification of heterogeneous degradation in Li-ion batteries, *Adv. Energy Mater.* 9 (2019), 1900674.
- [14] Y. Zhang, Z. Yang, C. Tian, Probing and quantifying cathode charge heterogeneity in Li ion batteries, *J. Mater. Chem.* 7 (2019) 23628–23661.
- [15] J.I.G. Dawkins, M.Z. Ghavidel, D. Chhin, I. Beaulieu, M.S. Hossain, R. Feng, J. Mauzeroll, S.B. Schougaard, Operando tracking of solution-phase concentration profiles in Li-ion battery positive electrodes using X-ray fluorescence, *Anal. Chem.* 92 (2020) 10908–10912.
- [16] J.D. Bazak, J.P. Allen, S.A. Krachkovskiy, G.R. Goward, Mapping of lithium-ion battery electrolyte transport properties and limiting currents with in situ MRI, *J. Electrochem. Soc.* 167 (2020), 140518.
- [17] H. Murayama, K. Kitada, K. Fukuda, A. Mitsui, K. Ohara, H. Arai, Y. Uchimoto, Z. Ogumi, E. Matsubara, Spectroscopic X-ray diffraction for microfocus inspection of Li-ion batteries, *J. Phys. Chem. C* 118 (2014) 20750–20755.
- [18] T. Nakamura, T. Watanabe, Y. Kimura, K. Amezawa, K. Nitta, H. Tanida, K. Ohara, Y. Uchimoto, Z. Ogumi, Visualization of inhomogeneous reaction distribution in the model LiCoO<sub>2</sub> composite electrode of lithium ion batteries, *J. Phys. Chem. C* 121 (2017) 2118–2124.
- [19] M.-T. von Sbrik, M. Marinescu, R.F. Martinez-Botas, G.J. Offer, A physically meaningful equivalent circuit network model of a lithium-ion battery accounting for local electrochemical and thermal behaviour, variable double layer capacitance and degradation, *J. Power Sources* 325 (2016) 171–184.
- [20] M. Quarti, W.G. Bessler, Model-based overpotential deconvolution, partial impedance spectroscopy, and sensitivity analysis of a lithium-ion cell with blend cathode, *Energy Technol.* 9 (2021), 2001122.
- [21] R. Xu, Y. Yang, F. Yin, P. Liu, P. Cloetens, Y. Liu, F. Lin, K. Zhao, Heterogeneous damage in Li-ion batteries: experimental analysis and theoretical modeling, *J. Mech. Phys. Solid.* 129 (2019) 160–183.
- [22] J. Nanda, J. Remillard, A. O'Neill, D. Bernardi, T. Ro, K.E. Nietering, J.Y. Go, T. J. Miller, Local state-of-charge mapping of lithium-ion battery electrodes, *Adv. Funct. Mater.* 21 (2011) 3282–3290.
- [23] H. Wang, Y. Zhu, S.C. Kim, A. Pei, Y. Li, D.T. Boyle, H. Wang, Z. Zhang, Y. Ye, W. Huang, Y. Liu, J. Xu, J. Li, F. Liu, Y. Cui, Underpotential lithium plating on graphite anodes caused by temperature heterogeneity, *Proc. Natl. Acad. Sci. USA* 117 (2020) 29453–29461.
- [24] M.J. Lain, J. Brandon, E. Kendrick, Design strategies for high power vs. high energy lithium ion cells, *Batteries* 5 (2019) 64.
- [25] W. Deng, W. Shi, Q. Liu, J. Jiang, X. Li, X. Feng, Constructing gradient porous structure in thick Li<sub>4</sub>Ti<sub>5</sub>O<sub>12</sub> electrode for high-energy and stable lithium-ion batteries, *ACS Sustain. Chem. Eng.* 8 (2020) 17062–17068.
- [26] X. Zhang, Z. Ju, Y. Zhu, K.J. Takeuchi, E.S. Takeuchi, A.C. Marschilok, G. Yu, Multiscale understanding and architecture design of high energy/power lithium-ion battery electrodes, *Adv. Energy Mater.* 11 (2021), 2000808.
- [27] S. Davidsson Kurland, Energy use for GWh-scale lithium-ion battery production, *Environ. Res. Commun.* 2 (2019), 012001.
- [28] J.S. Sander, R.M. Erb, L. Li, A. Gurijala, Y.M. Chiang, High-performance battery electrodes via magnetic templating, *Nat. Energy* 1 (2016), 16099.
- [29] J. Billaud, F. Bouville, T. Magrini, C. Villeveille, A.R. Studart, Magnetically aligned graphite electrodes for high-rate performance Li-ion batteries, *Nat. Energy* 1 (2016), 16097.
- [30] C. Huang, M. Dontigny, K. Zaghib, P.S. Grant, Low-tortuosity and graded lithium ion battery cathodes by ice templating, *J. Mater. Chem.* 7 (2019) 21421–21431.
- [31] Y. Qi, T. Jang, V. Ramadesigan, D. Schwartz, V. Subramanian, Is there a benefit in employing graded electrodes for lithium-ion batteries? *J. Electrochem. Soc.* 164 (2017) A3196–A3207.
- [32] Y.L. Dai, V. Srinivasan, On graded electrode porosity as a design tool for improving the energy density of batteries, *J. Electrochem. Soc.* 163 (2016) A406–A416.
- [33] E. Hosseinzadeh, J. Marco, P. Jennings, The impact of multi-layered porosity distribution on the performance of a lithium ion battery, *Appl. Math. Model.* 61 (2018) 107–123.
- [34] M. Wood, J. Li, Z. Du, C. Daniel, A.R. Dunlop, B.J. Polzin, A.N. Jansen, G. K. Krumdieck, D.L. Wood, Impact of secondary particle size and two-layer architectures on the high-rate performance of thick electrodes in lithium-ion battery pouch cells, *J. Power Sources* 515 (2021), 230429.
- [35] C. Cheng, R. Drummond, S. Duncan, P. Grant, Micro-scale graded electrodes for improved dynamic and cycling performance of Li-ion batteries, *J. Power Sources* 413 (2019) 59–67.

- [36] C. Cheng, R. Drummond, S. Duncan, P. Grant, Combining composition graded positive and negative electrodes for higher performance Li-ion batteries, *J. Power Sources* 448 (2020), 227376–227371–227311.
- [37] S. Kalnaus, K. Livingston, W.B. Hawley, H. Wang, J. Li, Design and processing for high performance Li ion battery electrodes with double-layer structure, *J. Energy Storage* 44 (2021), 103582.
- [38] X. Lu, A. Bertei, D.P. Finegan, C. Tan, S.R. Daemi, J.S. Weaving, K.B. O'Regan, T.M. M. Heenan, G. Hinds, E. Kendrick, D.J.L. Brett, P.R. Shearing, 3D microstructure design of lithium-ion battery electrodes assisted by X-ray nano-computed tomography and modelling, *Nat. Commun.* 11 (2020) 2079.
- [39] C. Huang, C.L.A. Leung, P. Leung, P.S. Grant, A solid-state battery cathode with a polymer composite electrolyte and low tortuosity microstructure by directional freezing and polymerization, *Adv. Energy Mater.* 2020 (2020), 2002387.
- [40] L. Liu, P. Guan, C. Liu, Experimental and simulation investigations of porosity graded cathodes in mitigating battery degradation of high voltage lithium-ion batteries, *J. Electrochem. Soc.* 164 (2017) A3163–A3173.
- [41] D. Westhoff, T. Danner, S. Hein, R. Scurtu, L. Kremer, A. Hoffmann, A. Hilger, I. Manke, M. Wohlfahrt-Mehrens, A. Latz, V. Schmidt, Analysis of microstructural effects in multi-layer lithium-ion battery cathodes, *Mater. Char.* 151 (2019) 166–174.
- [42] Y. Zhao, P. Stein, Y. Bai, M. Al-Siraj, Y. Yang, B.-X. Xu, A review on modeling of electro-chemo-mechanics in lithium-ion batteries, *J. Power Sources* 413 (2019) 259–283.
- [43] Y. Zhang, O.I. Malyi, Y.T. Tang, J. Wei, Z. Zhu, H. Xia, W. Li, J. Guo, X. Zhou, Z. Chen, C. Persson, X. Chen, Reducing the charge carrier transport barrier in functionally layer-graded electrodes, *Angew. Chem. Int. Ed.* 56 (2017) 14847–14852.
- [44] R. Drummond, C. Cheng, S.R. Duncan, P.S. Grant, Modelling the impedance response of graded LiFePO<sub>4</sub> cathodes for Li-ion batteries, *J. Electrochem. Soc.* 169 (2022), 010528.
- [45] L.-C. Chen, D. Liu, T.-J. Liu, C. Tiu, C.-R. Yang, W.-B. Chu, C.-C. Wan, Improvement of lithium-ion battery performance using a two-layered cathode by simultaneous slot-die coating, *J. Energy Storage* 5 (2016) 156–162.
- [46] V.R. Rikha, S.R. Sahu, A. Chatterjee, P.V. Satyam, R. Prakash, M.S.R. Rao, R. Gopalan, G. Sundarajan, In situ/ex situ investigations on the formation of the mosaic solid electrolyte interface layer on graphite anode for lithium-ion batteries, *J. Phys. Chem. C* 122 (2018) 28717–28726.
- [47] J.-F. Ding, R. Xu, C. Yan, B.-Q. Li, H. Yuan, J.-Q. Huang, A review on the failure and regulation of solid electrolyte interphase in lithium batteries, *J. Energy Chem.* 59 (2021) 306–319.
- [48] C. Huang, N.P. Young, J. Zhang, H.J. Snaith, P.S. Grant, A two layer electrode structure for improved Li Ion diffusion and volumetric capacity in Li Ion batteries, *Nano Energy* 31 (2017) 377–385.
- [49] C. Huang, A. Kim, D. Chung, E. Park, N. Young, K. Jurkschat, H. Kim, P. Grant, Multiscale engineered Si/SiO<sub>x</sub> nanocomposite electrodes for lithium-ion batteries using layer-by-layer spray deposition, *ACS Appl. Mater. Interfaces* 10 (2018) 15624–15633.
- [50] S. Lee, A. Mahadevegowda, C. Huang, J. Evans, P. Grant, Spray printing of self-assembled porous structures for high power battery electrodes, *J. Mater. Chem.* 6 (2018) 13133–13141.
- [51] S.H. Lee, C. Huang, P.S. Grant, High energy lithium ion capacitors using hybrid cathodes comprising electrical double layer and intercalation host multi-layers, *Energy Storage Mater.* 33 (2020) 408–415.
- [52] A.F. Léonard, N. Job, Safe and green Li-ion batteries based on LiFePO<sub>4</sub> and Li<sub>4</sub>Ti<sub>5</sub>O<sub>12</sub> sprayed as aqueous slurries with xanthan gum as common binder, *Mater. Today Energy* 12 (2019) 168–178.
- [53] J. Newman, K.E. Thomas-Alyea, *Electrochemical Systems*, third ed., Wiley, 2004.
- [54] G.W. Richardson, J.M. Foster, R. Ranom, C.P. Please, A.M. Ramos, Charge transport modelling of Lithium-ion batteries, *Eur. J. Appl. Math.* (2021) 1–49.
- [55] J. Wang, X. He, E. Paillard, N. Laszczynski, J. Li, S. Passerini, Lithium- and manganese-rich oxide cathode materials for high-energy lithium ion batteries, *Adv. Energy Mater.* 6 (2016), 1600906.
- [56] A.J. Bard, L.R. Faulkner, *Electrochemical Methods: Fundamentals and Applications*, John Wiley & Sons, New York, 2001.
- [57] J.E.B. Randles, A cathode ray polarograph. Part II.—the current-voltage curves, *Trans. Faraday Soc.* 44 (1948) 327–338.
- [58] A. Sevcik, Oscillographic polarography with periodical triangular voltage, *Collect. Czech Chem. Commun.* 13 (1948) 349–377.
- [59] D.Y.W. Yu, K. Donoue, T. Inoue, M. Fujimoto, S. Fujitani, Effect of electrode parameters on LiFePO<sub>4</sub> cathodes, *J. Electrochem. Soc.* 153 (2006) A835–A839.
- [60] D.Y.W. Yu, C. Fietzek, W. Weydanz, K. Donoue, T. Inoue, H. Kurokawa, S. Fujitani, Study of LiFePO<sub>4</sub> by cyclic voltammetry, *J. Electrochem. Soc.* 154 (2007) A253–A257.
- [61] R. de Levie, Electrochemical response of porous and rough electrodes, in: P. Delahay (Ed.), *Advances in Electrochemistry and Electrochemical Engineering*, Interscience, New York, 1967, pp. 329–397.
- [62] H. Zheng, R. Yang, G. Liu, X. Song, V.S. Battaglia, Cooperation between active material, polymeric binder and conductive carbon additive in lithium ion battery cathode, *J. Phys. Chem. C* 116 (2012) 4875–4882.
- [63] S. Ha, V.K. Ramani, W. Lu, J. Prakash, Optimization of inactive material content in lithium iron phosphate electrodes for high power applications, *Electrochim. Acta* 191 (2016) 173–182.
- [64] C. Wang, J. Hong, Ionic/electronic conducting characteristics of LiFePO<sub>4</sub> cathode materials, *Electrochem. Solid State Lett.* 10 (2007) A65–A69.